Adverse impact of terrain steepness on thermally-driven initiation of orographic convection

Matthias Göbel[1,2], Stefano Serafin[3], and Mathias W. Rotach[1]

[1]Department of Atmospheric and Cryospheric Sciences, University of Innsbruck, Innsbruck, Austria
[2]Regional Office Salzburg and Upper Austria, GeoSphere Austria, Salzburg
[3]Department of Meteorology and Geophysics, University of Vienna, Vienna, Austria

Correspondence: Matthias Göbel (matthias.goebel@geosphere.at)

Abstract. Diurnal mountain winds precondition the environment for deep moist convection through horizontal and vertical transport of heat and moisture. They also play a key role in convection initiation, especially in strongly inhibited environments, by lifting air parcels above the level of free convection. Despite its relevance, the impact of these thermally-driven circulations on convection initiation has yet to be examined systematically. Using idealized large-eddy simulations with the WRF model, we study the effect of cross-valley circulations on convection initiation under synoptically undisturbed and convectively inhibited conditions, considering quasi-2D mountain ranges of different heights and widths. In particular, we contrast convection initiation over relatively steep mountains (20 % average slope) and moderately steep ones (10 %). One distinctive finding is that, under identical environmental conditions, relatively steep mountain ranges lead to a delayed onset and lower intensity of deep moist convection, although they cause stronger thermal updrafts at ridge tops. This finding cannot be explained considering the temporal evolution of convective indices, such as convective inhibition and convective available potential energy. Analysis of the ridgetop moisture budget reveals the competing effects of moisture advection by the mean thermally-driven circulation and turbulent moisture transport. In general, at mountaintops, the divergence of the turbulent moisture flux offsets the convergence of the advective moisture flux almost entirely. The weaker total moistening found over steep mountains can be explained by considering that buoyant updrafts over their ridgetops are on average relatively narrow. Thus, they are more strongly affected by the turbulent entrainment of environmental air, which depletes their moisture and cloud water content and makes them less effective at initiating deep convection. In our simulations, convective updrafts over moderately steep mountains, on the other hand, gain more moisture from the vapor flux at cloud base and lose less moisture due to horizontal vapor fluxes over the course of the day, leading to significantly higher moisture accumulation. The precipitation efficiency, a measure of how much of the condensed water eventually precipitates, is also considerably larger over the moderately steep mountains. The weaker convection over steep mountains is a robust finding, valid over a range of background environmental stratifications and mountain sizes.

1 Introduction

Mountains are hotspots for the initiation of deep moist convection (DMC; Banta, 1990; Kirshbaum et al., 2018), which can result in thunderstorms with heavy precipitation in the form of rain and hail, lightning, and strong winds. The necessary (but

25   not sufficient) ingredients for its onset (Doswell et al., 1996) are a conditionally unstable environment, enough moisture for clouds and precipitation to form, and a lifting or triggering mechanism.

      In addition to synoptic-scale weather, mesoscale and boundary-layer processes in mountainous terrain can play an essential role in controlling these ingredients. Firstly, mountains act as a heat source that causes steep lapse rates in elevated mixed layers, which can be advected horizontally over nearby plains (e.g., Banacos and Ekster, 2010). Secondly, moisture often

30   accumulates over mountains due to the convergence of diurnal mountain winds (e.g., Demko et al., 2009). These occur on different spatial scales (e.g. as slope, valley, or mountain-plain breezes) and are induced by differential heating or cooling of the atmosphere relative to adjacent regions (Zardi and Whiteman, 2013). In some cases, the simultaneous occurrence of an elevated mixed layer and of low-level advection by the mountain-plain breeze creates optimal conditions for organized intense convection, such as supercell storms, at mountain foothills (Scheffknecht et al., 2017).

35   Besides transporting heat and moisture, diurnal mountain winds lead to uplift in convergence areas, providing a mechanism for the thermal forcing of orographic convection initiation (CI). Another orographic CI mechanism is forced uplifting of the airflow, which is a purely mechanical forcing that occurs irrespective of differential heating. Past research focused mostly on the latter process, as reviewed e.g. by Houze (2012) and Colle (2013).

      Banta (1990) and more recently Kirshbaum et al. (2018) presented extensive overviews of mechanical and thermal forcing

40   and their interaction. The impact of thermal circulations on CI can be especially large during periods of weak synoptic flow with large values of convective inhibition (CIN). Strongly inhibited environments require considerable lifting for CI to take place, so they delay or even completely prevent convection onset, even in the presence of large convective available potential energy (CAPE). This type of convection is referred to as non-equilibrium convection (Done et al., 2006), as opposed to equilibrium convection where CAPE is quickly consumed by DMC after its creation, for instance during the passage of a cold front.

45   Non-equilibrium convection is associated with lower predictability, especially when convection is parameterized (Done et al., 2006, 2012; Zimmer et al., 2011; Keil et al., 2014).

      The important and sometimes subtle role that diurnal mountain winds play in CI has been shown in several field campaigns and related modeling studies. Demko and Geerts (2010) simulated a convective day during the CuPIDO campaign (Damiani et al., 2008) in Arizona, confirming that DMC originated along a convergence line formed by the slope wind circulation, and

50   moved downwind afterward. While the upslope flow provided the necessary moisture for DMC, it also cooled the air above the ridge. Thus, when upslope winds weakened after the convective episode and their advective cooling effect vanished, renewed convection was initiated after local destabilization (boundary-layer thermals reaching the level of free convection, LFC).

      In the Convective and Orographically-induced Precipitation Study (COPS, Wulfmeyer et al., 2011) in southwestern Germany and eastern France, a large fraction of the observed convective events was triggered above mountainous terrain (the Black For-

55   est) due to thermal forcing. A climatology of radar reflectivity in the same region, spanning eight summer seasons (Weckwerth et al., 2011), revealed that twice as many convective events were initiated over the mountainous terrain than over the Rhine valley in the study period. On average, convection events also grew larger, more intense, and longer-lived over the mountains. The peak in convective activity was found to be around local noon, coincident with the period of most intense orographically-induced convergence. Manzato et al. (2022) came to similar conclusions in a 15-year climatology of cloud-to-ground lightning

60 flash density over the Alpine area. They showed that lightning is less frequent on average over the main Alpine ridge than over the surrounding plains. However, they also demonstrated that CI takes place preferentially over elevated areas, more frequently in the afternoon, and that the higher flash density over plains is often due to the downstream propagation of mature storms that originated over the mountains.

In recent years, the field campaigns RELAMPAGO (Nesbitt et al., 2021) and CACTI (Varble et al., 2021) focused on under-
65 standing the mechanisms of CI and upscale development around the Sierras de Córdoba in Argentina. DMC frequently initiates here, aided by the convergence of upslope flows, and rapidly grows upscale to yield supercells and mesoscale convective systems (Mulholland et al., 2018), often resulting in large hail (Kumjian et al., 2020; Bechis et al., 2022). Marquis et al. (2021) found that the observable quantity that most clearly differentiates between cases of sustained and unsustained precipitation was the depth of the horizontal convergence zone. Nelson et al. (2022) designed idealized simulations to interpret cases where CI
70 failed to occur in a supportive environment. They demonstrated that these events were affected by the relatively low relative humidity of the environmental air above the lifting condensation level (LCL), which favored the dilution of buoyant thermals by turbulent entrainment. The authors also found that, in the presence of converging thermally-driven upslope flows, much narrower boundary-layer thermals were sufficient to yield CI. Another modeling study related to RELAMPAGO showed that higher mountains resulted in stronger upslope flows and thus earlier CI (Mulholland et al., 2020).

75 The ability of diurnal mountain wind systems to lift air parcels above the LFC and thus trigger DMC depends on various governing parameters such as the surface energy balance, the local thermodynamic profile, background winds, and terrain geometry.

The surface energy balance controls the very existence of thermal circulations. The main drivers are solar forcing and soil moisture. The latter influences the partitioning of the available net radiation into latent and sensible heat fluxes. The vertical
80 mass transport operated by orographic thermally-driven circulations depends on the balance between the energy input supplied by the surface sensible heat flux and the energy required to destabilize the atmospheric column (Leukauf et al., 2016). Stronger heat flux or weaker low-level stability imply increased turnover of the low-level atmosphere, and hence increased vertical transport of any trace constituent, such as moisture. However, if the moisture content is high enough for cloud formation, cloud cover alters the surface energy balance, weakening both surface fluxes and thermal circulations.

85 Besides stability, another property of the thermodynamic profile that received considerable attention in recent studies on orographic CI is relative humidity. Its vertical variability is thought to play a key role in controlling whether or not destabilization will occur (Kirshbaum, 2011; Nelson et al., 2022). High values of surface relative humidity lower the LCL and generally also the LFC, facilitating CI. Thermal circulations enhance the moisture content close to the surface by mass and thus moisture convergence. However, the surface-based vertical updrafts that compensate for low-level convergence lose moisture and buoy-
90 ancy while ascending through a drier environment, because of turbulent mixing. In principle, shallow convection can lessen the detrimental effects of dry entrainment by progressively moistening the environment during the course of the diurnal cycle, facilitating the transition towards DMC (Kirshbaum, 2011).

The presence and strength of background winds have multiple implications. Strong background winds intensify turbulence and entrainment, and they also vent away thermals before an organized updraft can form. They are thus in principle detrimental

95   to CI at mountain tops (Kirshbaum, 2011). An environmental wind can also displace thermal updrafts from the mountaintop towards the lee side, creating an asymmetric pressure field that enhances moisture flux convergence at the leeward foothills (Panosetti et al., 2016). This process effectively shifts the preferential CI location leeward of the mountain tops, but it is sensitive to mountain height (it seemingly does not occur over shallow mountains). It is also sensitive to stratification, as documented by Hagen et al. (2011).

100   Besides wind speed, the wind direction relative to a mountain ridge matters as well. Crook and Tucker (2005) and Tucker and Crook (2005) found that vertical uplift, and thus the ability to initiate moist convection, is maximized over mountain ranges oriented along rather than across the incoming wind direction, because of the more favorable interaction between crosswise thermally-driven convergence and streamwise mechanically-forced displacement of the flow. Soderholm et al. (2013) pointed out that directional wind shear is important as well. Vertically uniform wind direction above a ridge implies that the warm and

105   moist storm inflow will be eventually undercut by the gust front, leading to short-lived convection. If the wind blows along the ridge at low levels and across it higher up, the previously described negative feedback is disrupted, and the likelihood of sustained convection is increased.

    Compared with the role of atmospheric properties, the impact of terrain morphology on CI has attracted much less attention. Imamovic et al. (2019) investigated the impact of terrain geometry on DMC under weak synoptic forcing and low CIN using

110   idealized simulations with $\Delta x = 1$ km. They found a linear relationship between rain amounts and mountain volume in a surprisingly large portion of the governing parameter space—excluding situations with strong background winds or large mountains. This relationship only arises in a statistical sense, as the variability among equivalent model runs is enormous. Imamovic et al. (2019) explain the observed linear scaling as a consequence of larger mountains driving stronger thermal circulations, and they speculate that the relationship would break down in cases with relatively high CIN.

115   Strongly inhibited conditions are by no means exceptional. For instance, according to long-term analyses of radiosoundings in the Alpine region (e.g., Manzato, 2003), persistent CAPE is not accessible due to high CIN for more than half of the time during the convective season. Therefore, in this study, we continue investigating the impact of terrain geometry on orographic CI and take a closer look at strongly inhibited conditions. We use idealized large-eddy simulations (LES) to investigate the sensitivity of the slope wind system and of the ridgetop moisture budget to the slope angle. We further explain the implications

120   for the initiation and intensity of DMC and the additional impacts of mountain height and initial stratification.

2   Methods

We performed LES simulations with the Advanced Research (ARW) dynamical solver of the Weather Research and Forecasting (WRF) model version 4.3.1 (Skamarock and Klemp, 2008). The WRF model is an open-source community model suitable for multiple scales ranging from LES to global simulations. It integrates the fully-compressible, non-hydrostatic Euler equations

125   in flux form with tendencies from subgrid-scale processes. The model uses a pressure-based vertical coordinate named η with a smooth transition from terrain-following at lower levels to isobaric higher up (hybrid sigma-pressure vertical coordinate, Klemp, 2011). A horizontally and vertically staggered grid is used for spatial discretization, whereby the horizontal grid is of

Arakawa-C type. By default, the advection is fifth-order in the horizontal and third-order in the vertical. For the integration in time, the WRF model uses a 3rd-order Runge-Kutta scheme and integrates acoustic modes on fractional steps (Wicker and

130 Skamarock, 2002). Model configurations common to all our model runs are described in Sect. 2.1 and 2.2. The whole set of simulations, which comprises both dry and moist model runs and considers mountains of different widths and heights, is introduced in detail in Sect. 2.3.

2.1 Model configuration

Our discretization uses a horizontal grid spacing of $\Delta x = 100$ m and a time increment of $\Delta t = 1$ s. We use a positive-definite

135 advection scheme for scalars and Weighted Essentially Non-Oscillatory (WENO, Liu et al., 1994) advection for momentum variables. We simulate moist airflow over a mountain ridge. Since we use periodic lateral boundary conditions, the ridge is infinitely long in the y-direction and repeated infinitely in the x-direction as a series of valleys and ridges. In the x-direction, the domain size equals the mountain width w_m, which varies between simulations. In the y-direction, it is 40 km, which is enough to achieve robust along-valley averages of turbulence statistics and precipitation amounts, and a clear ordering of the

140 simulations in terms of initiation time and intensity of deep moist convection.

In the vertical, there are 253 levels with Δz between ~ 20 m near the ground and ~ 100 m from 12 km height to the model top at about 17 km height (details about the vertical grid are given in Appendix A). For the dry simulations (see Sect. 2.3), in which deep moist convection does not develop, we lowered the model top to 8 km with 102 vertical levels. Implicit Rayleigh damping (Klemp et al., 2008) with a damping coefficient of 0.2 s^{-1} is used above a height of 12 km (6 km for the dry

145 simulations) to prevent vertically-propagating gravity waves from being reflected at the model top.

The effects of Coriolis force and curvature on the momentum budget are neglected, because of the small extent of the studied phenomenon and the associated high Rossby number. Subgrid-scale mixing is described with the well-established 1.5-order TKE scheme by Deardorff (1980). Turbulent fluxes in the surface layer are modeled with the revised MM5 similarity theory scheme (Jiménez et al., 2012). Microphysical processes are handled by the *Predicted Particle Properties* (P3, Morrison and

150 Milbrandt, 2015) parameterization, a bulk scheme that complements the usual conservation equation for cloud ice mass with additional prognostic quantities, i.e., rimed mass, rimed volume, and number concentration.

To enable realistic interactions between the surface energy balance, surface winds, and precipitation, the setup of the land surface model and the radiative transfer parameterization required some attention. We used the NOAH land surface model (Chen and Dudhia, 2001) and considered grassland land cover, with an albedo of 0.19 and a vegetation fraction of 80%. The

155 soil texture type is loam. Radiation was modeled by an improved version of the Rapid Radiative Transfer Model for GCMs (RRTMG-K, Baek, 2017), setting the latitude to 47.7°N and the day of the year to 15 July for reasons explained in Sect. 2.3. As a simplification, neither orographic shading nor slope-dependent radiation was considered, leading to uniform surface forcing on slopes with different angles and orientations. For the moist simulations, this configuration led to domain-averaged diurnal peak values of net shortwave radiation, sensible heat flux, and latent heat flux, respectively, of ~ 750 W m^{-2}, ~ 130 W m^{-2}

160 and ~ 400 W m^{-2} (a Bowen ratio of about 0.33).

2.2 Initialization

All model integrations are started at 6 LT (local solar time), about one hour after sunrise, and run until 19 LT. The starting time is chosen to lie within the morning transition period, during which the reversal of slope wind direction occurs and the intensity of thermally-induced winds is low. To perturb the initial state and initiate convection, random potential temperature perturbations

165 are introduced. The perturbations are uniformly distributed with a maximum amplitude of 0.1 K and applied equally to the lowest 12 model levels ($\sim$ 260 m) based on Kealy et al. (2019). As suggested by Kealy et al. (2019), we use vertically uniform initial perturbations, which are less susceptible to numerical dissipation during model spin-up and are therefore more effective at triggering convective circulations.

At model initialization, the temperature gradient at the interface between the ground and the atmosphere is set to zero by

170 equating the skin temperature to the atmospheric temperature extrapolated to the ground. This ensures that the surface sensible heat flux at the beginning of the simulation is equal to zero at all grid points, thereby avoiding the development of spurious thermal circulations. The deep soil temperature varies with elevation in a manner compatible with climatological values in central Europe. The soil temperature is then linearly interpolated to the surface; the linear temperature profile in the soil ensures that also the ground heat flux is initially zero.

175 Following Schlemmer et al. (2011), the soil moisture saturation ratio increases quadratically from 60% at the surface to 75% at the lowest soil level at a depth of 1.5 m.

2.3 Simulation series

The initial thermodynamic profiles of all our simulations are shown in Fig. 1. They are based on an idealized version of a radiosounding from the intensive observational period (IOP) 8b of COPS. The radiosonde was launched on 15 July 2007 at 08:00

180 UTC (09:00 CET) from Burnhaupt Le Bas in the southern part of the Rhine Valley and characterizes the pre-convective environment. In the early afternoon of that day, a mesoscale convergence zone interacted with diurnal mountain wind circulations and enhanced low-level uplift, triggering deep moist convection over the Black Forest despite high CIN and only moderate CAPE values (Kalthoff et al., 2009). An idealized version of this sounding was first used by Kirshbaum (2011) and later by Panosetti et al. (2018). In this study, we introduce several modifications of the COPS IOP8b sounding, which ensure that the

185 environment where ridgetop thermal plumes ascend has comparable properties across all simulations, despite differences in the terrain geometry.

We prescribed the model orography with a cosine profile:

$$h(x) = \frac{h_{\mathrm{m}}}{2}\left[1 + \cos\left(\frac{2\pi x}{w_m}\right)\right] \tag{1}$$

and carried out simulations with different mountain heights h_{m} and widths w_{m}. We used mountain heights of 500 m and

190 1000 m (low and high mountain) and average slope angles of 10 % and 20 % (moderate and steep mountain) by changing w_{m} accordingly. The chosen values are roughly representative of the hilly terrain of the Black Forest region and are shown in Fig. 2 and Table 1. The terrain is homogeneous in the y-direction, which implies that no along-valley pressure gradient and no along-valley flow can develop in the simulations. This enables us to study the effects of cross-valley flows in isolation.
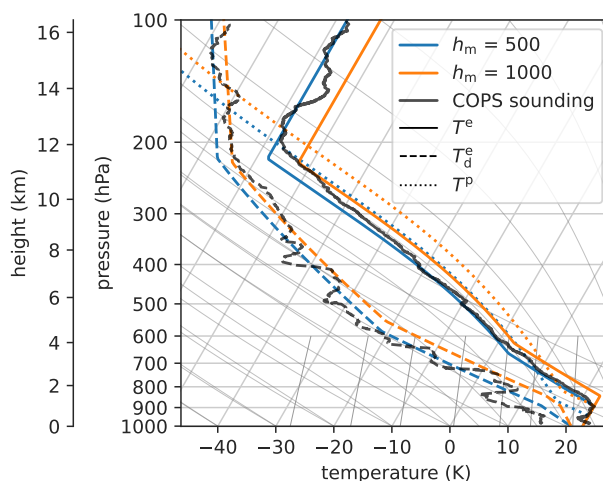
Figure 1. SkewT-diagrams of the initial environment and parcel profiles for the moist simulation series. The solid lines show the environment temperature profiles (T^e), the dashed lines are the environment dewpoint temperature profiles (T^e_d), and the dotted lines are the temperature profiles of parcels (T^p) rising from the surface of the mountain ridges with height h_m. The black lines are the temperature and dewpoint profiles of the observed COPS sounding that our cases are based on (see text in Sect. 2.3).
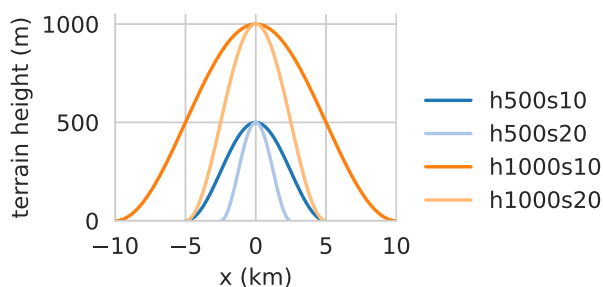
Figure 2. Orography of the performed simulations.

Table 1 gives an overview of all simulations and their characteristics. Initial profiles are designed so that CAPE, CIN, and the height of the LFC above the mountaintop are roughly equal in all simulations. This ensures that the destabilization of the column requires the same energy input and the intensity of the resulting convection is similar in all simulations. Of course, this is expected to be only approximately true, because destabilization occurs on a fairly long time scale (a few hours), during which the atmospheric state adjusts to the evolving surface energy balance.

In all simulations a ground-based stable (isothermal) layer extends up to 500 m above the ridge, followed by a near-neutral layer up to 3000 m above the ridge, and a pseudo-adiabatic layer up to the tropopause at 11.5 km AMSL (see Table 2). The stratosphere has an isothermal stratification. The initial dewpoint profiles are also constructed relative to the mountain heights

Table 1. Setup and characteristics of the moist simulations. The given convective indices refer to a surface parcel rising from the mountain ridge at model starting time. h_s refers to the depth of the ground-based stable layer.

terrain	h_m	avg. slope	w_m	h_s	CIN	CAPE	LCL	LFC	LNB	mean RH below LFC
	(m)	(%)	(km)	(m)	(J kg^{-1})	(J kg^{-1})	(m a.g.l.)	(m a.g.l.)	(km a.g.l.)	(%)
h500s10	500	10	10	1000	154	1547	727	1887	11.5	54
h500s20	500	20	5	1000	154	1546	727	1887	11.5	54
h1000s10	1000	10	20	1500	152	1542	746	1861	11.1	53
h1000s20	1000	20	10	1500	152	1542	746	1861	11.1	53

Table 2. Initial temperature gradients. The initial surface temperature is 296 K.

Height interval (m)	$\partial_z T$ (K km^{-1})
$[0, h_m + 500]$	0
$[h_m + 500, h_m + 3000]$	-8
$[h_m + 3000, 11500]$	pseudo-adiabatic
$[11500, 17000]$	0

(see Table 3). In this way, the initial temperature and dewpoint profiles above the ridge as a function of height above ground are almost identical up to the tropopause for all simulations.

The whole set of simulations was repeated with greatly reduced moisture content to study the full diurnal cycle of the cross-valley circulation without interference from clouds and precipitation. For these dry simulations, the initial dewpoint is reduced by 14 K at all levels.

3 Results

3.1 Circulation intensity and convection initiation

For an overview of the cross-valley circulations that develop in the simulations, we first look at y-averaged cross-sections. Figure 3 shows water vapor mixing ratio, potential temperature, wind vectors, and cloud contours at 11 LT. The high-mountain simulations develop two stacked circulation cells, while the low-mountain simulations only have one large circulation cell. This feature is also found in simulations by Wagner et al. (2015), where stacked circulation cells appeared only for mountain heights of 1500 m and more. Likely, the critical mountain height for stacked circulations is dependent on valley width, stratification, and heat input. Intuitively, weaker stratification and stronger heat input lead to deeper mixing in a shorter time yielding a single

Table 3. Initial dewpoint gradients. The initial surface dewpoint is 294 K for the moist and 280 K for the dry simulations.

| | $\partial_z T_{\mathrm{d}}$ (K km^{-1}) | |
Height interval (m)	$h_m = 500$ m	$h_m = 1000$ m
$[0, h_m]$	-7.3	-3.8
$[h_m, h_m + 500]$	-6.8	-7
$[h_m + 500, h_m + 4000]$	-10	-10
$[h_m + 4000, 11500]$	-6.5	-6.5
$[11500, 17000]$	-3	-3
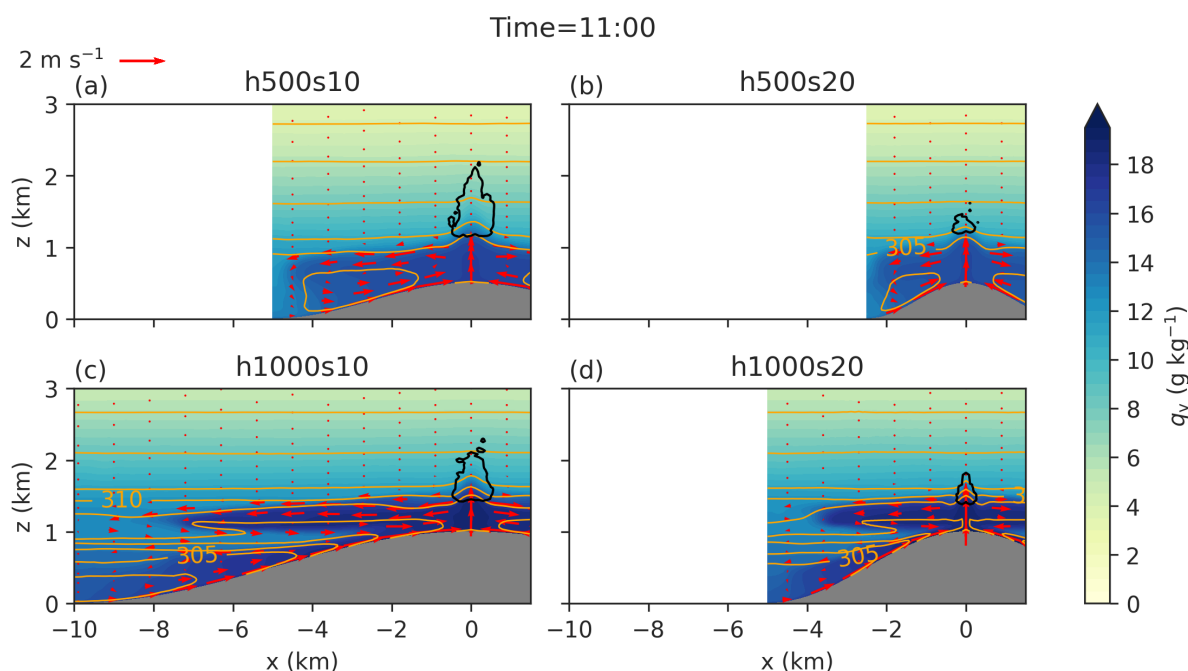
Figure 3. y-averaged cross-sections of the moist simulation series with water vapor mixing ratio (shaded), wind vectors, and potential temperature contours (spacing of 1 K) at 11 LT for (a) the h500s10, (b) h500s20, (c) h1000s10, and (d) h1000s20 simulations. The black contour line marks cloud water mixing ratio values above 1 mg kg^{-1}.

215   circulation cell. With a constant initial potential temperature gradient $\partial_z \theta_0$ of 3 or 4 K km^{-1} (weaker stratification compared with the isothermal temperature profile) we also obtain single circulation cells only (not shown).

     In Fig. 3 we also see that the clouds develop faster in the moderately steep simulations, h500s10 and h1000s10. These simulations also feature an earlier onset of precipitation and much higher total precipitation sums than the steep runs, h500s20 and h1000s20 (Fig. 4a). The h500s20 simulation has hardly any precipitation. The spatial distribution of precipitation is similar
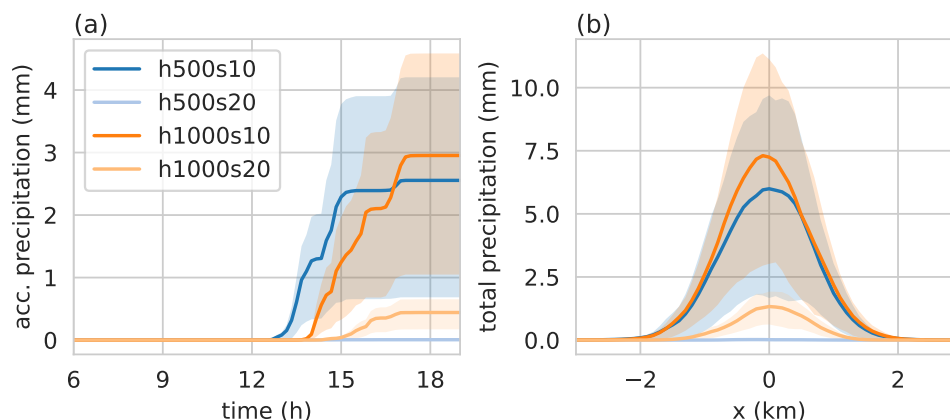
Figure 4. Accumulated precipitation in the four simulations (colored lines), (a) averaged in y and $x \in [-2 \text{ km}, 2 \text{ km}]$ as a function of time; (b) at simulation end, averaged in y as a function of x. Shading indicates the variability (interquartile range) in the y-direction.

220 over the low and high moderate mountains although the high mountain is twice as wide as the low mountain: The precipitation is largest over the ridge and tends to zero (< 1 % of its maximum value) about 2 km away from it following a Gaussian curve (Fig. 4b). In Fig. 4a, the h1000s10 simulation shows the largest total precipitation averaged over $x \in [-2 \text{ km}, 2 \text{ km}]$. The data shown in Fig. 4 and all following figures are averaged in the y-direction. The shading indicates the variability (interquartile range) in the y-direction.

225 To understand the differences in convection initiation between the simulations, we first consider classical convective indices such as CAPE, CIN, LCL above ground level, and LFC above ground level for a surface parcel uplifted from the ridge top before precipitation onset (Fig. 5; lines in the figure terminate at the time precipitation reaches the ground). Diurnal heating, erosion of the surface-based stable layer, and moisture convergence at the mountaintop imply that CIN decreases and CAPE increases during the course of the day. When the instability is gradually released in form of cloud development, CAPE is 230 reduced again. The evolution of LCL and LFC is mainly driven by the evolution of relative humidity closely above the ridge. The relative humidity first shows a sharp increase until about 8 LT (decrease of LCL and LFC), followed by a gradual decrease (increase of LCL and LFC). Thus, until 8 LT the moistening due to surface evaporation and the convergence of the mean circulation is dominant, while later in the day the warming of the air overcompensates the effect of the moistening and causes the decrease in relative humidity.

235 By design, the initial values of convective indices are about the same in all simulations. After about 8:30 LT, the LFC and LCL are much closer to the mountaintop in the high-mountain simulations (h1000), which, however, does not lead to an earlier onset of precipitation. The time when CIN reaches values close to zero is not well correlated with the precipitation onset either. Precipitation onset follows CIN removal by a lag between 3 hours (for the h500s10 simulation) and 5 hours (for the two high-mountain simulations). Consequently, the h500s10 simulation has the earliest onset of precipitation although its CIN 240 reaches zero relatively late. Also, the maximum value of CAPE is not well correlated with the total amount of precipitation
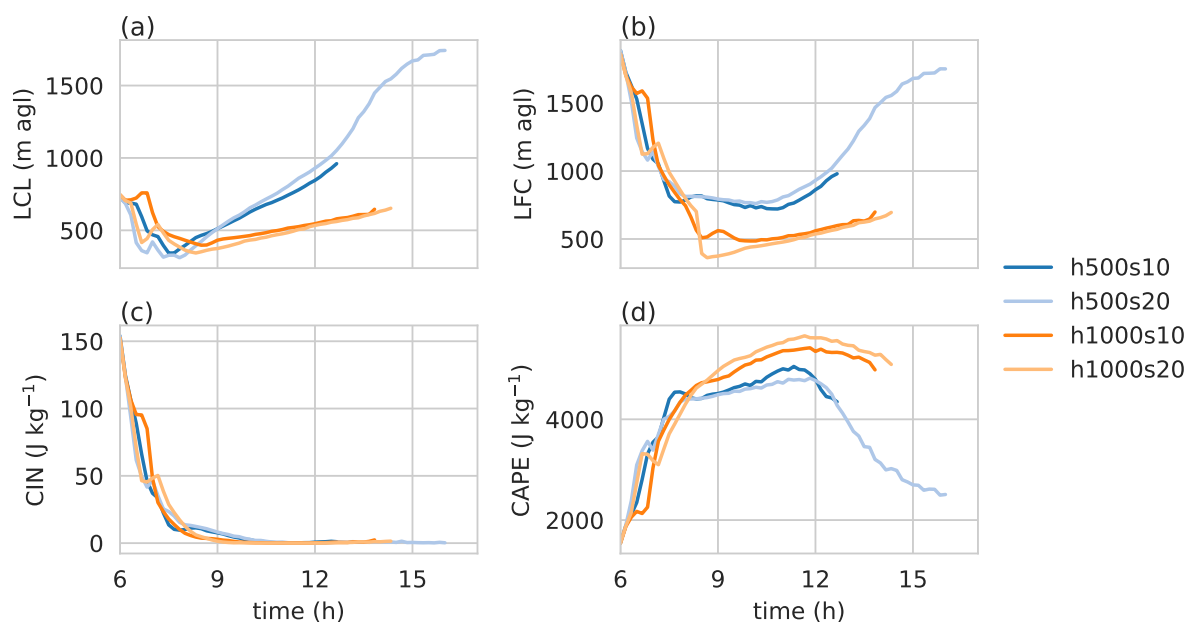
Figure 5. Evolution of (a) LCL (above ground level), (b) LFC (above ground level), (c) CIN, and (d) CAPE for surface parcels starting at the ridge before precipitation onset. Precipitation onset is defined as the time when domain-averaged accumulated precipitation reaches 0.01 mm.

(compare Fig. 5d with Fig. 4). An exception is the h500s20 simulation, which produces almost no precipitation, CAPE values are lowest and CIN drops the latest to zero. In all other cases, there is no systematic link between the value and temporal trends of convective indices and the onset and amount of precipitation.

As convective indices do not help to understand the differences between the simulations, we examine the intensity of the
245   cross-valley circulation as quantified by the strength of the updraft over the ridge, w_{max}. Figure 6 shows the maximum vertical velocity in the vertical column above the ridge (one grid point in x-direction) for the dry and moist simulations. w_{max} is first calculated for each grid point in y-direction and then averaged in y-direction. In the dry simulations, the circulation is stronger in the s20 runs except for a short period in the early morning. In the moist simulations, we can see the sudden strengthening of the updraft due to the latent heat released by cloud formation, which happens generally after 11 LT and earliest in the
250   h500s10 case. The h500s20 case that hardly developed any precipitation still shows a considerable increase in vertical velocity due to latent heating. The question remains, why the s20 simulations (over relatively steep terrain) develop later and weaker DMC compared with the s10 simulations, despite their thermal updrafts being persistently stronger around the time of cloud formation and precipitation onset. To answer this question we investigate the moisture budget above the ridge.
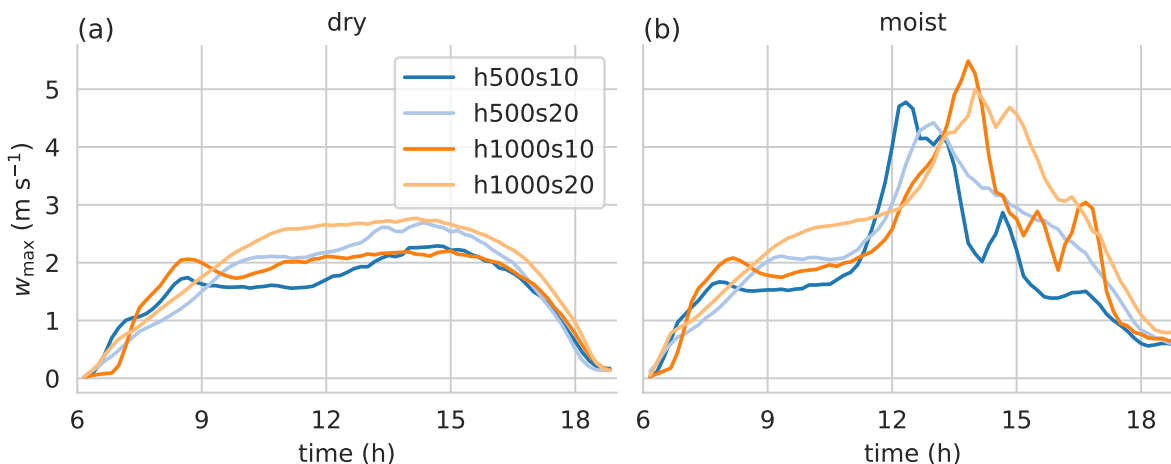
Figure 6. Time series of maximum vertical velocity in the vertical column above the ridge (one grid point in x-direction) for (a) the dry and (b) the moist runs (30-min moving average).
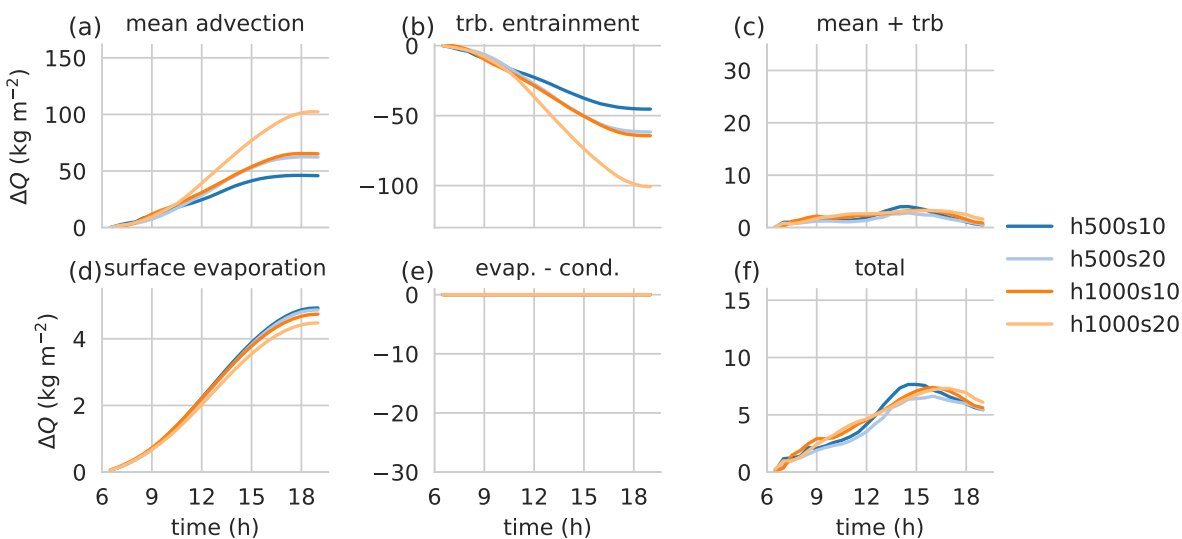
Figure 7. Time series of vertically and temporally integrated water vapor budget components above the ridge calculated with Eq. 2 for the dry runs. The panels show (a) mean advection, (b) turbulent entrainment, (c) sum of mean advection and turbulent entrainment, (d) surface evaporation, (e) net evaporation (evaporation - condensation), and (f) total moistening.

3.2 Moisture budget

255 The budget calculations were performed with the WRFlux online tendency and flux averaging tool (Göbel et al., 2022), version 1.3.2 (Göbel, 2021). All moisture budget components are averaged in time during model integration using 30-min block
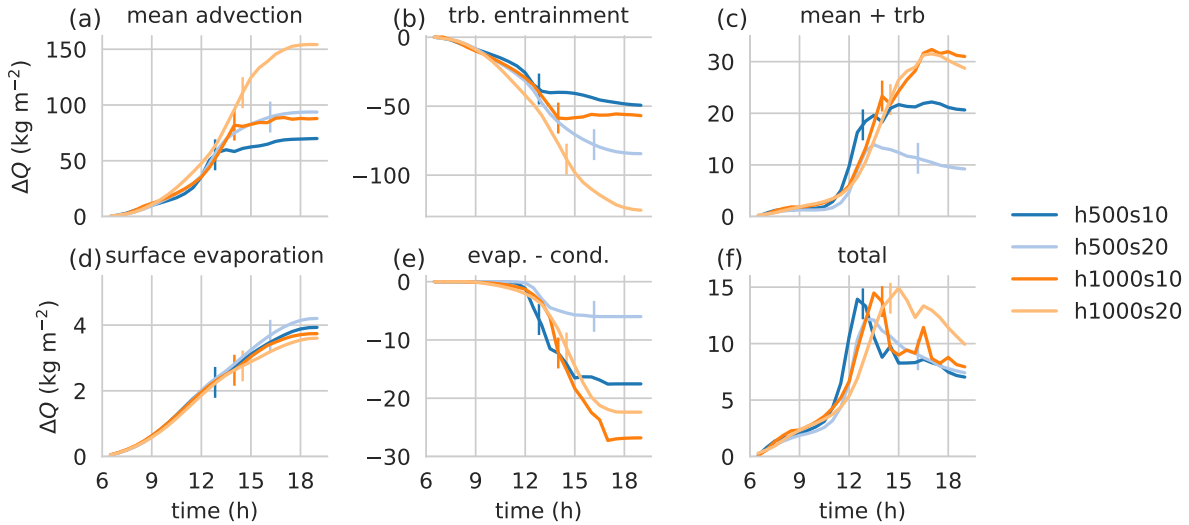
Figure 8. As Fig. 7 but for the moist runs. The vertical lines mark the precipitation onset, that is the time when domain-averaged accumulated precipitation reaches 0.01 mm.

averages. In the postprocessing, the advection is decomposed into mean, resolved turbulent, and subgrid-scale turbulent components (see Schmidli, 2013; Göbel et al., 2022). We compute the cumulative change in y-averaged, vertically integrated water vapor content between the surface z_0 and the model top z_{top}:

$$
260 \quad \Delta Q(x,t) = \frac{1}{L_y} \int_{t_0}^{t} \int_{0}^{L_y} \int_{z_0}^{z_{\mathrm{top}}} \frac{\partial \rho q_{\mathrm{v}}}{\partial t} \, \mathrm{d}z \, \mathrm{d}y \, \mathrm{d}t' = Q_t - Q_0 \tag{2}
$$

The budget consists of surface evaporation (not integrated vertically), mean advection, horizontal turbulent entrainment (resolved and subgrid-scale), and the microphysics tendency (evaporation + sublimation − condensation − deposition).

Figure 7 shows the moisture budget components for the dry simulations above the ridge. The moistening due to surface evaporation is very similar for all simulations (Fig. 7d). In contrast, the stronger circulation in the s20 runs leads to a stronger
265 moistening due to the mean advective component compared with the respective s10 runs (Fig. 7a). The mean advective tendency is at least one order of magnitude larger than surface evaporation. However, it is offset almost entirely by drying due to turbulent entrainment (Fig. 7b). The final moisture tendency is again of much smaller overall magnitude and very similar for all simulations (Fig. 7f). Surface evaporation amounts to about 20% of the total moistening in the early stages of the simulation, but the ratio increases to between 70 and 90% towards the end of the day. The h500s10 case shows slightly more moistening than the h500s20 simulation which can at least partly explain why the convection is much more intense in the former. On
270 the other hand, there is hardly any difference between the high-mountain simulations. Because moisture accumulation at the mountaintop follows a nearly identical trend in all dry simulations, most likely it will not explain the differences in initiation time and intensity of convection in the moist simulations.
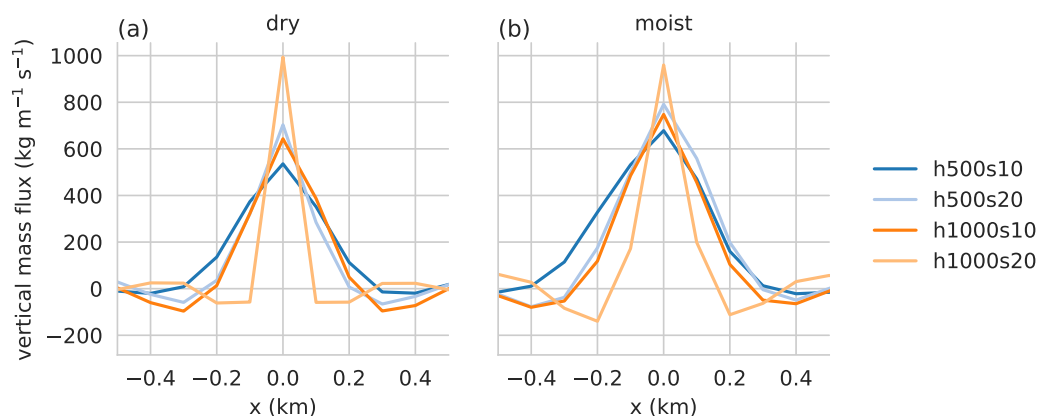
Figure 9. Vertical mass flux integrated vertically for (a) the dry and (b) the moist runs as a function of x at 11 LT.

The moisture budget for the moist runs is shown in Fig. 8. The net advective tendency (Fig. 8c) arising from the counteracting

275   effects of mean advection and turbulent entrainment is much higher than in the dry runs. The resulting excess moisture is partly

compensated by net condensation starting at around noon (Fig. 8e). Overall, there is a strong gain in moisture content above

the ridge (Fig. 8f) due to the strengthening of the circulation after 11 LT when clouds start to form (Fig. 8a), followed by a

decrease in moisture due to continued condensation (Fig. 8e) and the disruption of the cross-valley circulation by precipitation

(marked with vertical lines in Fig. 8).

280   So far, the strength of the circulation was only quantified in terms of the updraft velocity directly over the ridge. Figure 9

shows the y-averaged vertically integrated vertical mass flux at 11 LT as a function of x. Updrafts are significantly broader

over the moderately steep mountains compared with the respective steep mountains: The updraft width over the moderately

steep mountains, computed by finding the roots in Fig. 9 with linear interpolation, is larger by 38 % (dry) and 34 % (moist) for

the low mountains and 136 % (dry) and 68 % (moist) for the high mountains. The smaller cross-section of the updrafts over

285   steeper mountains makes them more susceptible to the entrainment of dryer, non-cloudy air, which weakens them. In fact, the

h500s10 case that has the earliest onset of DMC has the weakest (on the ridge) but widest updraft of all simulations. As cloud

formation and latent heat release already started at 11 LT (Figs. 3 and 8e), the updrafts are somewhat wider and stronger in the

moist simulations compared with the dry ones.

The narrower updrafts over the steep mountains can also be seen in Fig. 10 which shows again the vertically and temporally

290   integrated water vapor budget components for the moist runs now as a function of x at 12 LT. At mountaintop ($x = 0$), the mean

advective moistening and the drying due to turbulent entrainment are stronger in the s20 than in the respective s10 simulations.

However, at some distance from the mountain top ($100 \leq |x| \leq 500$ m), these budget components are much stronger in the

s10 simulations, where convective updrafts are wider. The total moisture tendency is considerably larger for the moderately

steep mountains everywhere within about 1 km from the ridge, owing to the more favorable balance between mean advection
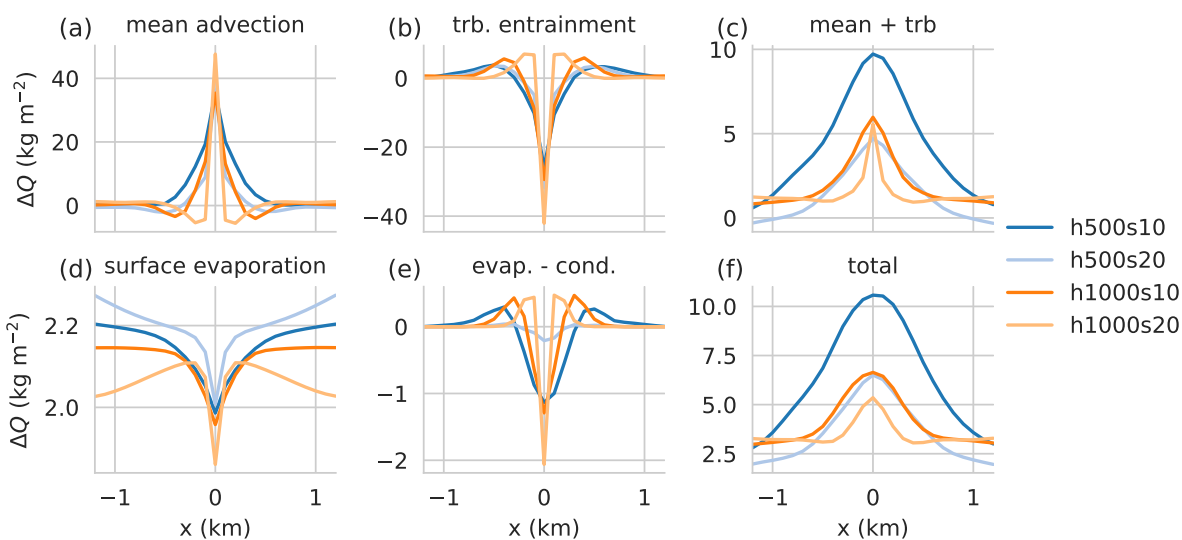
Figure 10. As Fig. 8 but as a function of x at 12 LT.

and turbulent entrainment. h500s10 has the largest total moistening at 12 LT which is connected with it having the earliest precipitation onset (see Fig. 4).

We therefore hypothesize that the earlier onset and higher amount of precipitation observed in the s10 runs are linked with the mean updraft size. If the whole updraft width is considered, the rate of advective moisture transport over the ridge in the s10 runs is higher and is counteracted by weaker turbulent dilution than in the respective s20 runs. Broader updrafts, which form preferentially over the less sharp orographic profile of the s10 runs, are thus more likely to evolve into precipitating cumulonimbus clouds.

4 Discussion

In this section, we discuss the robustness of our findings with respect to some aspects of the initial conditions (Sect. 4.1) and investigate the precipitation process in more detail. For the latter purpose, we assess precipitation efficiency (Sect. 4.2) and determine how the precipitation scales with the mountain volume (Sect. 4.3). We also link these findings to previous literature.

4.1 Sensitivity to convective inhibition and a broader range of mountain geometries

To estimate the robustness of our results, we ran some simulations with the same terrain configuration but a less stable stratification. We changed the temperature gradient in the first layer from isothermal to -3 K km^{-1} and in the second layer to -7.1 K km^{-1}. For the h500 simulations, the surface temperature in the valley is 296 K, as before. For the h1000 simulations, it is raised to 297.5 K to obtain the same temperature at the mountaintop as in the low-mountain simulations. The dewpoint profiles remain the same as before. With this new stratification, initial CIN is reduced to 73 J kg^{-1} (roughly half compared with before),
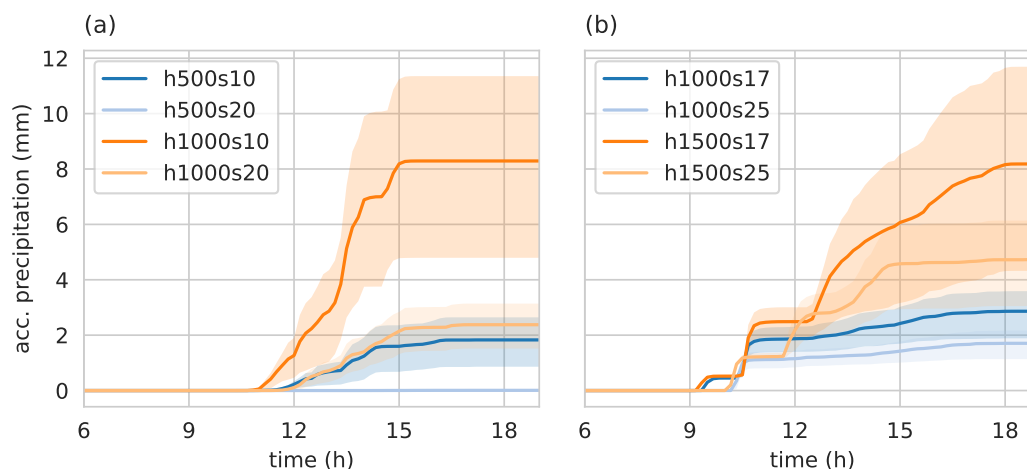
Figure 11. As Fig. 4a, but (a) for runs with lower initial CIN (LCIN) and (b) for runs with adjusted mountain height h and slope s and adjusted initial profiles so that the mountain protrudes the stable layer. Simulations in (b) were run with $\Delta x = 250$ m.

while initial CAPE stays about the same. Therefore we call these simulations the LCIN simulations and the original ones the HCIN simulations.

We also investigated cases where the model orography corresponds more closely to typical alpine mountain ranges. These
315 are generally higher and steeper than the Black Forest hills, which inspired the simulations described so far. In these additional cases, the mountain ridge reaches 500 m above the stable layer using mountain heights of 1000 m and 1500 m combined with average slopes of about 17 and 25%. The model is run with $\Delta x = 250$ m. For brevity, we omit details about the model settings and the initial profiles. The namelist files and input soundings are available on Zenodo (Göbel, 2023).

The additional simulations described in this section are not listed in Table 1 but the nomenclature for the terrain (consisting
320 of mountain height X and slope Y: hXsY) is the same.

Figure 11a shows the accumulated precipitation for the LCIN simulations. As expected, precipitation starts earlier in the LCIN (between 11 and 12 LT) than in the HCIN simulations (between 12 and 15 LT, Fig. 4). While the total amount of precipitation is considerably increased for the high-mountain simulations, it is decreased for the h500s10 case. The h500s20 case again produces hardly any precipitation. Thus, the conclusion that the steeper mountains lead to later and weaker DMC is
325 also valid for more unstable simulations.

The circulation intensity in the dry LCIN simulations is similar to the dry HCIN simulations, with a stronger but narrower updraft for the steep runs. The updrafts are slightly stronger and wider compared with the original runs (not shown).

Figure 11b shows the accumulated precipitation for the higher and steeper simulations with $\Delta x = 250$ m. Also in these simulations the conclusion still remains the same: steeper mountains lead to later and weaker convection.
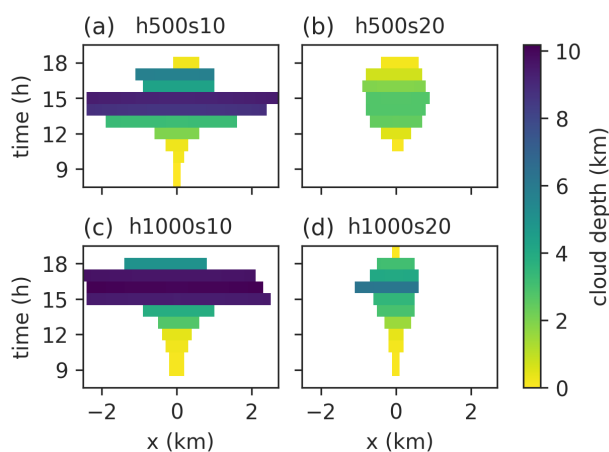
Figure 12. Depth and horizontal extent of the active cloud developing with time for (a) the h500s10, (b) h500s20, (c) h1000s10, and (d) h1000s20 simulations.

4.2 Cloud water budget and precipitation efficiency

In Sect. 3 we demonstrated that orographic convection over mountains of moderate steepness is connected with an earlier onset and a higher accumulation of rainfall. We interpreted this finding as a consequence of a more favorable balance between moisture advection due to the thermally-driven circulation and moisture diffusion due to turbulence, which results in a stronger accumulation of water vapor at the mountaintop. This finding is in line with recent research emphasizing that dry air entrainment plays a key role in determining the fate of moist updrafts (Nelson et al., 2022; Marquis et al., 2021; Kirshbaum, 2011). Here we demonstrate that updraft dilution ultimately results in a reduction of the precipitation efficiency, i.e., the fraction of condensed water mass that actually precipitates to the ground (Demko and Geerts, 2010). For this purpose, we complement the preceding treatment of the water vapor budget (Sect. 3) with an analysis of the cloud water budget.

Following Demko and Geerts (2010) we specify a cloud control volume, wherein we perform a total water (vapor, liquid, and solid) budget analysis at hourly intervals. The definition of the cloud control volume is based on the average water vapor tendency by the microphysics scheme (evaporation + sublimation − condensation − deposition) within the last hour. It spans the whole simulation domain in the y-direction and its cross-section corresponds to the smallest rectangle (in the $x - \eta$ plane) containing all grid points with y-averaged microphysics tendency less than -10^{-8} s^{-1} (significant net condensation/deposition). Inactive cloud parts (no significant net condensation/deposition) that have been advected away from the cloud core region are thus excluded. The vertical boundaries are defined along η-levels (vertical model levels in WRF) instead of constant height levels to avoid numerical inaccuracies in the budget caused by interpolation. Water vapor and hydrometeors can be transported laterally across the cloud volume boundaries by advection and turbulent exchange. The cloud volume grows in time horizontally and vertically as shown in Fig. 12, most noticeably in the s10 simulations. Figure 13 illustrates the definitions of the active cloud volume and the different cloud water budget components. The cloud volume gains water by the vertical vapor flux
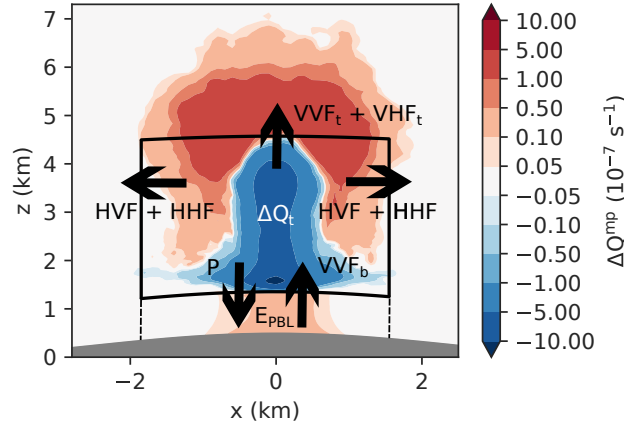
Figure 13. Concept of the cloud water budget. The shading indicates the average water vapor tendency by the microphysics scheme between 12 and 13 LT in the h500s10 simulation. The black box is the active cloud volume. The cloud water budget (vapor, liquid, and solid) consists of the horizontal vapor flux HVF, the vertical vapor fluxes at cloud base and top VVF_b and VVF_t, the horizontal hydrometeor flux HHF, the vertical hydrometeor flux at cloud top VHF_t, the surface precipitation P, the precipitation that evaporates below cloud base (between the dashed lines) E_{PBL}, and the total change of cloud water ΔQ_t.

at cloud base (VVF_b) and loses water due to the horizontal fluxes of vapor (HVF) and hydrometeors (HHF), the respective vertical fluxes at cloud top (VVF_t and VHF_t), precipitation that reaches the ground (P) and precipitation that evaporates below cloud base (E_{PBL}). The total water tendency is denoted with ΔQ_t. ΔQ_t also contains the change in total water content due to the change of the size of the cloud volume alone (ΔQ_t^{VC}). This component is also treated as a source (or loss) term for Q_t.

We computed the different budget components from the output of our budget analysis tool WRFlux (HVF, $VVF_{b/t}$, E_{PBL}) and from standard WRF output (P, ΔQ_t, ΔQ_t^{VC}). In contrast to Demko and Geerts (2010), we accumulated the values over the whole simulation time instead of using hourly aggregates since in our case the precipitation is considerably delayed with respect to the moisture accumulation. In the y-direction, all components are averaged, not integrated, since the domain length in the y-direction is arbitrary. Therefore, the budget components are given in kg m^{-1}.

E_{PBL} is computed by integrating the y-averaged net evaporation rate E (in kg m^{-3} s^{-1}) below cloud base:

$$E_{PBL} = \int_{t_0}^{t} \int_{x_1}^{x_2} \int_{z_0}^{z_1} E \, dz \, dx \, dt' \tag{3}$$

where x_1 and x_2 denote the left and right boundaries of the cloud volume, respectively, and $z_1 = z_1(x, \eta_1)$ is the height of the lower boundary (height of model level η_1 at x).

Since the fluxes of hydrometeors are not tracked in WRFlux, we deduced HHF and VHF_t from two hydrometeor mass budgets $\partial_t Q_H$ outside the cloud volume. The only relevant terms in these budgets are HHF (VHF_t) and the net evaporation left

and right of (above) the cloud volume. Hence,

$$\text{HHF} = -\int_{t_0}^{t}\int_{-L_x/2}^{x_1}\int_{z_0}^{z_{\text{top}}}(\partial_t Q_{\text{H}} + E)\,\mathrm{d}z\,\mathrm{d}x\,\mathrm{d}t'$$
$$-\int_{t_0}^{t}\int_{x_2}^{L_x/2}\int_{z_0}^{z_{\text{top}}}(\partial_t Q_{\text{H}} + E)\,\mathrm{d}z\,\mathrm{d}x\,\mathrm{d}t' \tag{4}$$

and

$$\text{VHF}_{\text{t}} = -\int_{t_0}^{t}\int_{x1}^{x_2}\int_{z_2}^{z_{\text{top}}}(\partial_t Q_{\text{H}} + E)\,\mathrm{d}z\,\mathrm{d}x\,\mathrm{d}t' \tag{5}$$

where $z_2 = z_2(x, \eta_2)$ is the height of the upper boundary of the cloud volume and L_x the domain with.

The temporally accumulated cloud water budget components are shown in Fig. 14. All budget components are defined as being positive when they are a gain for total water in the cloud volume. RES denotes the residual of the budget, i.e.

$$\text{RES} = \Delta Q_{\text{t}} - (\text{HVF} + \text{HHF} + \text{VVF}_{\text{b}} + \text{VVF}_{\text{t}}$$
$$+\text{VHF}_{\text{t}} + \text{P} + \text{E}_{\text{PBL}} + \Delta Q_{\text{t}}^{\text{VC}}). \tag{6}$$

RES is small compared with the other shown components but not completely negligible.

The main source term VVF_{b} is largely but not entirely compensated by HVF. VVF_{t} is also negative but with a relatively small magnitude since vertical velocities are small at cloud top (not shown). The moderately steep mountains drive a stronger cloud base moisture flux than the respective steep mountains. Therefore, and due to a decreased outflow of HVF later in the day, the net advective water vapor tendency ($\text{HVF} + \text{VVF}_{\text{b}} + \text{VVF}_{\text{t}}$) at the end of the day is 2.5 to 3 times as large for the two moderately steep mountains compared with the two steep mountains (Fig. 14c). Thus, as stated earlier, the moist updrafts over the moderately steep mountains are, due to their larger size, less susceptible to the entrainment of dry environmental air.

Figure 15 shows vertical profiles of the anomalies of water vapor mixing ratio and vertical velocity in the cloud control volume (black box in Fig. 13) at 12 LT. Anomalies are defined as differences between the x- and y-averaged vertical profiles in the cloud volume (averaged on constant height levels) and the corresponding profiles in the surrounding environment. The stronger moistening in the s10 cases is clearly visible. This is in line with results by Griewank et al. (2022), who also diagnosed larger moisture anomalies in relatively wide convective updrafts in large-eddy simulations, but referring to the boundary layer over flat terrain (Southern Great Plains, US). They also documented larger vertical velocity anomalies in the wider updrafts, which contrasts with our findings in Fig. 15b. Griewank's anomaly profiles are derived from a population of 3D cloud objects, while we consider a specific cloud control volume spanning the whole domain length in y-direction. Thus, the observed discrepancies might result from the differences in the analysis methods, but possibly also from a fundamental difference between convection over flat and mountainous terrain.

According to Demko and Geerts (2010) the precipitation efficiency can be estimated as $\text{P}/\text{VVF}_{\text{b}}$, since VVF_{b} can be seen as an estimate for the condensation (without evaporation) in the cloud. Using the accumulated values at the end of the simulation
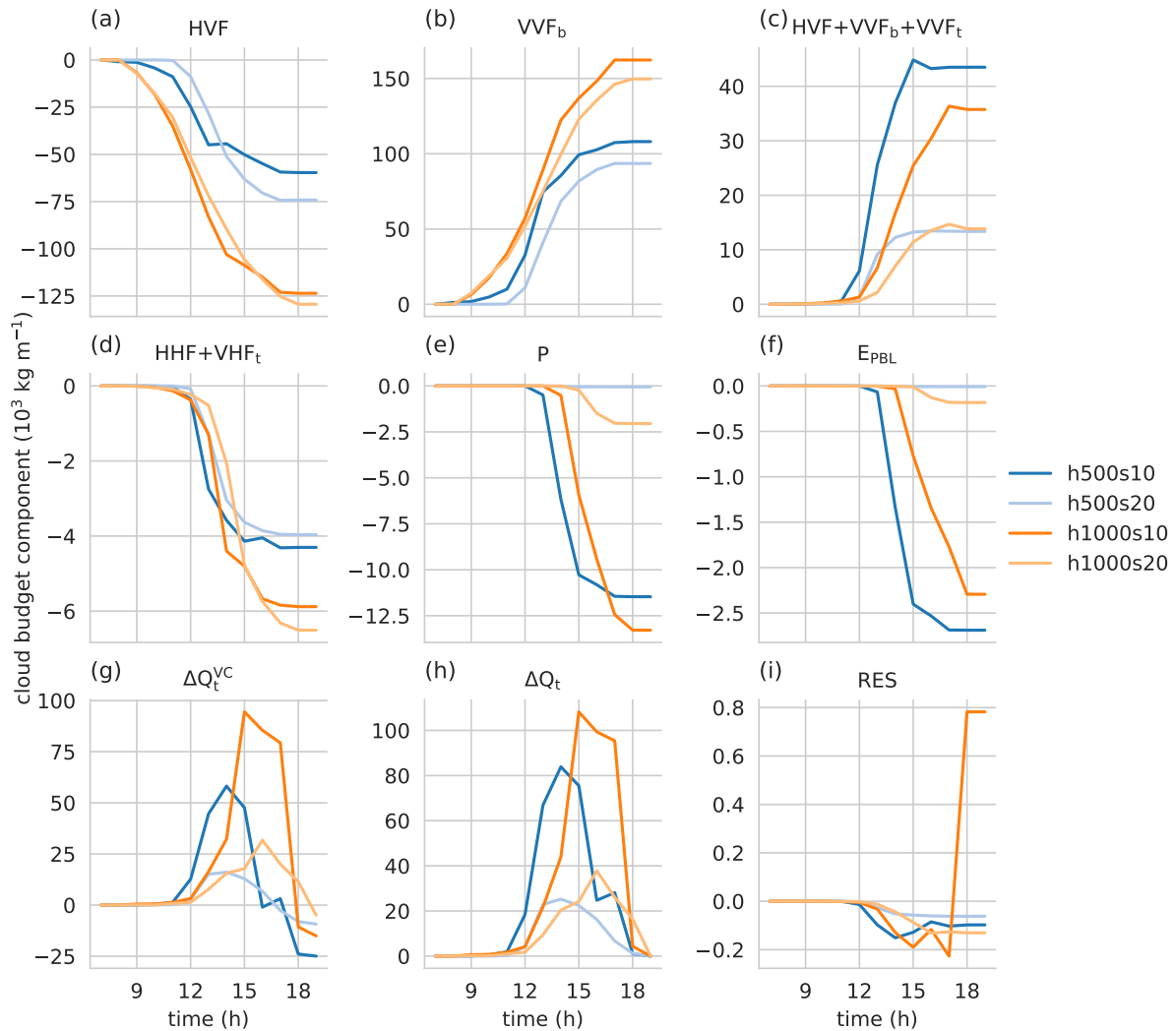
Figure 14. Timeseries of the accumulated cloud water budget components. Positive values indicate a gain of total water (vapor, liquid, and solid) in the cloud volume. The panels show (a) the horizontal vapor flux HVF, (b) the vertical vapor flux at cloud base $\mathrm{VVF_b}$, (c) the sum of horizontal and vertical vapor fluxes $\mathrm{HVF+VVF_b+VVF_t}$ ($\mathrm{VVF_t}$: vertical vapor flux at cloud top), (d) the sum of horizontal and cloud-top vertical hydrometeor fluxes $\mathrm{HHF+VHF_t}$, (e) the surface precipitation P, (f) the precipitation that evaporates below cloud base E_{PBL}, (g) the change of cloud water due to volume change $\Delta Q_{\mathrm{t}}^{\mathrm{VC}}$, (h) the total change of cloud water ΔQ_{t}, and (i) the residual RES.

leads to a precipitation efficiency of 11.5 %, 0.04 %, 7.7 %, and 1.2 % for the h500s10, h500s20, h1000s10, and h1000s20 simulations, respectively. The h500s10 can thus be called the most efficient in terms of precipitation production. The s20 simulations are very inefficient at producing precipitation. Demko and Geerts (2010) found hourly precipitation efficiencies of

395 up to 1 % in the shallow convective period and up to 42 % for the deep convective period with an average of 9 %, which is
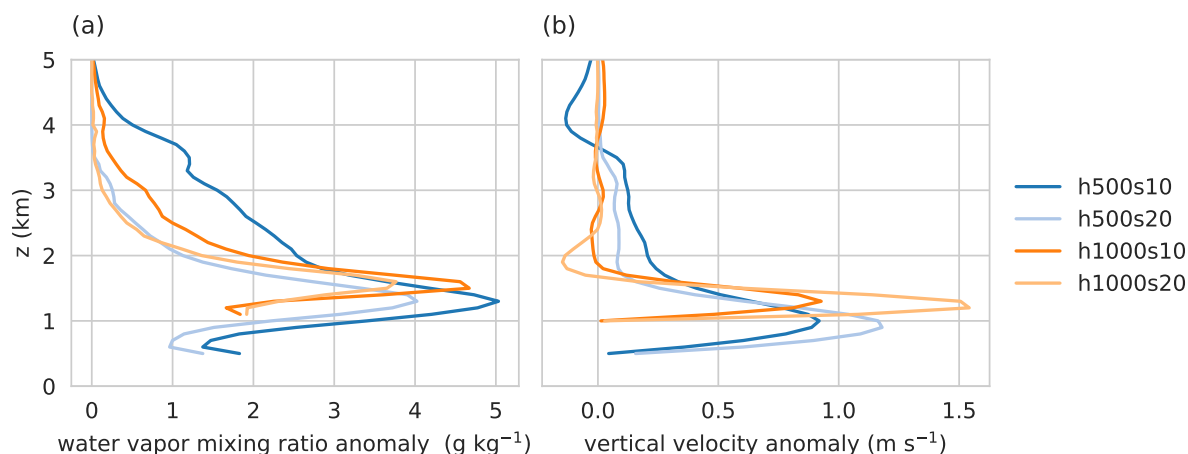
Figure 15. Profiles of water vapor mixing ratio anomaly (a) and vertical velocity anomaly (b) of the active cloud with respect to the surrounding environment in the moist runs at 12 LT.

roughly in line with our time-integrated values for the moderately steep mountains. However, the whole simulation setup and also the calculation of precipitation efficiency are rather different in their case, so a good agreement is not necessarily expected.

In summary, the cloud water budget thus provides an additional explanation for why precipitation is delayed and reduced over steep mountains. First, less water vapor accumulates in the active cloud volume before precipitation begins, as demonstrated
400 in Sect. 3.2. Second, a smaller fraction of the water vapor that enters the cloud base is actually converted into precipitation, as demonstrated here.

4.3   Volume scaling

Figure 16 shows normalized total domain-averaged precipitation P/P_0 as a function of normalized terrain volume V/V_0 for all LCIN and HCIN simulations. Following Imamovic et al. (2019), we choose a reference simulation for which $P = P_0$
405 and $V = V_0$ (h1000s20 LCIN in our case), and we evaluate how P/P_0 depends on V/V_0. Imamovic et al. (2019) found a linear relationship between P/P_0 and V/V_0 in a weakly inhibited environment. Our LCIN simulations show a monotonic relationship that is also close to linear when the smallest mountain is excluded. Doubling the volume leads to an increase in precipitation with factors 1.25 (h1000s20 vs h500s10) and 1.77 (h1000s10 vs h1000s20), which is roughly the same as in Fig. 7b of Imamovic et al. (2019) (reproduced in the gray line in Fig. 16). As Imamovic et al. (2019) speculated, this monotonic
410 relationship does not hold in our strongly inhibited HCIN simulations. The s10 simulations ($V/V_0 = 0.5$ and 2) both produce more precipitation than the h1000s20 mountain ($V/V_0 = 1$).

Due to the low initial CIN in their simulations, Imamovic et al. (2019) still observed significant precipitation amounts for low mountain volumes and even for flat terrain, while we obtained hardly any precipitation for our smallest mountain ($V/V_0 = 0.25$, h500s20, both LCIN and HCIN).
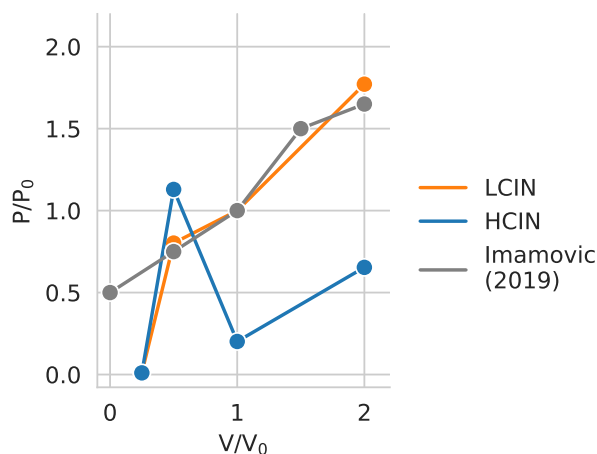
Figure 16. Total domain-averaged precipitation P as a function of terrain volume V (equivalent to cross-sectional area) normalized by the values for the h1000s20 LCIN simulation (P_0 and V_0) for the runs with lower (LCIN) and higher (HCIN) initial CIN. The gray line is based on Imamovic et al. (2019, their Fig. 7b).

5 Conclusions

We performed idealized LES simulations with the WRF model to study the effect of thermally-induced cross-valley circulations on convection initiation for different mountain heights and widths, under synoptically undisturbed and convectively inhibited conditions. We found that mountain geometry has a significant impact on convection initiation time and strength. Steeper mountains lead to a later onset and lower intensity of deep moist convection despite the stronger associated thermally-driven circulation. The apparent discrepancy is explained by the behavior of convective updrafts on mountain tops, which are the focal points of the convective destabilization. Thermal plumes atop steeper mountains gain more moisture by mean moisture convergence. However, they are also narrower and thus lose more moisture and cloud droplets due to entrainment. The latter seems to be a more important effect in our case. We obtained these results considering mountains with heights between 500 and 1000 m and half-widths between 5 and 10 km and a nearly isothermal temperature profile at all heights up to 500 m above the mountaintop (and conditional instability further aloft). However, we verified that the findings are robust also for more unstable stratification and/or slightly higher and steeper mountains.

While classical convective indices like LCL, LFC, CIN, and CAPE are not very informative in this case, analysis of the circulation and the water vapor and total cloud water budgets above the ridge provides valuable insight into the differences between the simulations. The moisture tendency at the mountaintop is not driven purely by the strength of the mean circulation. Actually, before condensation starts, moistening due to the convergence of advective fluxes is almost entirely compensated by drying due to turbulent entrainment. A stronger circulation can lead to smaller total moistening if turbulent entrainment of dry air prevails, as found for instance for our h500s20 mountain compared with the h500s10 mountain. When clouds start

to form, the circulation generates a higher net advective tendency (mean + turbulent), which is then compensated partly by condensation.

435 Based on Demko and Geerts (2010), we developed a novel approach to quantify the components of the water budget for a convective cloud using the output of the online tendency and flux averaging tool WRFlux (Göbel et al., 2022). The extent of the cloud is defined using a threshold for the net condensation rate to exclude inactive parts of the cloud. In our simulations, convective updrafts over moderately steep mountains gain more moisture from the vapor flux at cloud base and lose less moisture due to horizontal vapor fluxes over the course of the day, leading to significantly higher moisture accumulation. The

440 precipitation efficiency, a measure for how much of the condensed water eventually precipitates, as derived from the cloud water budget, is also considerably larger over the moderately steep mountains.

The accumulated precipitation amount in the highly inhibited conditions we studied is apparently controlled by mountain steepness, but not by mountain size. For instance, we found no evidence of the nearly linear scaling between precipitation amount and mountain volume documented by Imamovic et al. (2019) in weakly inhibited convective regimes.

445 In this study, we only investigated highly idealized orographies. As a next step, semi-idealized simulations with realistic 3D orography as in Weinkaemmerer et al. (2023) and heterogeneous land cover or soil moisture can provide further valuable insights into the sensitivity of convection to mountain geometry. The interactions between cross-valley circulation, valley winds, plain-to-mountain winds, and an upper-level, large-scale wind add to the complexity that needs to be investigated with 3D orographies. The background wind impact might be the most critical. Intuitively, large-scale advection can either enhance

450 or counteract moisture accumulation at mountain tops, depending on how moist or dry the incoming air is. In any case, it would tend to make the horizontal moisture distribution less dependent on the underlying orography, possibly canceling the steepness effect we documented.

To connect insights from idealized simulations with real-world processes, an analysis of the terrain geometry around hotspots in convection initiation climatologies (e.g., from radar reflectivity or lightning frequency) can also be investigated.

455 Our results have a possibly important implication. If vertical mass transport at mountain tops is, all other factors equal, systematically affected by orographic sharpness, then it is nearly impossible for operational-scale numerical weather prediction models to resolve it correctly. In fact, the model orography is invariably much more regular than the actual one, not only because it is sampled at discrete points, but also because it is artificially smoothed to prevent numerical instability. Thus, novel approaches for the parameterization of boundary-layer transport over mountains, accounting for sub-grid-scale orographic

460 complexity, are likely needed.

Appendix A: Vertical grid

The vertical grid in our simulations consists of two layers comprising in total n_z grid points. In the first layer, $0 < z < z_1$, vertical grid increments Δz_i increase smoothly from $\Delta z_{\min} = 20$ m to $\Delta z_{\max} = 100$ m, as prescribed by:

$$\Delta z_{\mathrm{i}} = \Delta z_{\mathrm{m}} + \frac{\Delta z_{\min} - \Delta z_{\mathrm{m}}}{\tanh(2)} \tanh\left(4\frac{2\mathrm{i} - n_z}{2 - n_z}\right) \tag{A1}$$

465 for $i = 1, ..., n_z - 1$ with

$$\Delta z_{\mathrm{m}} = \frac{\Delta z_{\min} + \Delta z_{\max}}{2}. \tag{A2}$$

In the second layer, $z_1 < z < z_{\mathrm{top}}$, $\Delta z_{\mathrm{i}} = \Delta z_{\max}$. This definition is inspired by one of the options available in the ARPS model (Xue et al., 2000) and leads to a strong increase of Δz with height and leveling off towards z_1.

Since the η vertical coordinate in WRF is pressure-based, we transform the nominal height levels z_i to nominal pressure

470 levels p_i assuming hydrostatic balance in the initial potential temperature profile.

Further, we convert to nominal η_i terrain-following levels with $\eta_i = (p_i - p_{\mathrm{top}})/(p_s - p_{\mathrm{top}})$, using $p_s = p_0 = 1000$ hPa for the surface pressure. These η_i values span the $[0, 1]$ range. Because p_s varies markedly with terrain elevation and is generally smaller than p_0, a given $\Delta \eta_i$ corresponds to a smaller height increment over elevated terrain. The η coordinate is hybrid terrain-following, becoming isobaric above height z_{hyb}.

475 In the moist simulations $n_z = 253$, $z_1 = 12$ km, $z_{\mathrm{top}} = 17$ km, and $z_{\mathrm{hyb}} = 10$ km. In the dry simulations $n_z = 102$, $z_1 = 3$ km, $z_{\mathrm{top}} = 8$ km and $z_{\mathrm{hyb}} = 6$ km.

Code and data availability. The y-averaged model output, namelist and input sounding files, and the code to reproduce the simulations, the figures and the input soundings are available on Zenodo (Göbel, 2023). The simulations can be reproduced using WRFlux v1.3.2 (Göbel, 2021) and the modified source code files from Göbel (2023).

480 *Author contributions.* MG developed the concept, ran and analyzed the simulations, and prepared the manuscript. StS and MWR supervised the work and reviewed and edited the paper extensively. StS acquired the funding and administers the project.

Competing interests. The authors declare that they have no conflict of interest.

Acknowledgements. This work is funded by the Austrian Science Fund (FWF) research project P30808-N32 "Multiscale Interactions in Convection Initiation in the Alps". The computational results presented have been achieved using the Vienna Scientific Cluster (VSC) and

485 the LEO cluster of the University of Innsbruck. Matthias Göbel thanks Wiebke Scholz for her support and the various fruitful discussions.

References

Baek, S.: A Revised Radiation Package of G-packed McICA and Two-Stream Approximation: Performance Evaluation in a Global Weather Forecasting Model, J. Adv. Model Earth Sy., 9, 1628–1640, https://doi.org/10/gbr4m4, 2017.

Banacos, P. C. and Ekster, M. L.: The Association of the Elevated Mixed Layer with Significant Severe Weather Events in the Northeastern United States, Wea. Forecasting, 25, 1082–1102, https://doi.org/10.1175/2010WAF2222363.1, 2010.

Banta, R. M.: The Role of Mountain Flows in Making Clouds, in: Atmospheric Processes over Complex Terrain, pp. 229–283, Springer, 1990.

Bechis, H., Galligani, V., Alvarez Imaz, M., Cancelada, M., Simone, I., Piscitelli, F., Maldonado, P., Salio, P., and Nesbitt, S. W.: A Case Study of a Severe Hailstorm in Mendoza, Argentina, during the RELAMPAGO-CACTI Field Campaign, Atmos. Res., 271, 106 127, https://doi.org/10.1016/j.atmosres.2022.106127, 2022.

Chen, F. and Dudhia, J.: Coupling an Advanced Land Surface–Hydrology Model with the Penn State–NCAR MM5 Modeling System. Part I: Model Implementation and Sensitivity, Mon. Wea. Rev., 129, 569–585, https://doi.org/10/c6m89k, 2001.

Colle, B. A.: Theory, Observations, and Predictions of Orographic Precipitation, in: Theory, Observations, and Predictions of Orographic Precipitation, vol. Mountain Weather Research and Forecasting, pp. 291–344, Springer, https://doi.org/10.1007/978-94-007-4098-3_6, 2013.

Crook, N. A. and Tucker, D. F.: Flow over Heated Terrain. Part I: Linear Theory and Idealized Numerical Simulations, Mon. Wea. Rev., 133, 2552–2564, https://doi.org/10/b8v2dx, 2005.

Damiani, R., Zehnder, J., Geerts, B., Demko, J., Haimov, S., Petti, J., Poulos, G. S., Razdan, A., Hu, J., Leuthold, M., and French, J.: The Cumulus, Photogrammetric, In Situ, and Doppler Observations Experiment of 2006, Bull. Amer. Meteor. Soc., 89, 57–74, https://doi.org/10/cmzqz3, 2008.

Deardorff, J. W.: Stratocumulus-Capped Mixed Layers Derived from a Three-Dimensional Model, Bound-lay. Meteorol., 18, 495–527, https://doi.org/10/dtgccs, 1980.

Demko, J. C. and Geerts, B.: A Numerical Study of the Evolving Convective Boundary Layer and Orographic Circulation around the Santa Catalina Mountains in Arizona. Part II: Interaction with Deep Convection, Mon. Wea. Rev., 138, 3603–3622, https://doi.org/10/ct25m6, 2010.

Demko, J. C., Geerts, B., Miao, Q., and Zehnder, J. A.: Boundary Layer Energy Transport and Cumulus Development over a Heated Mountain: An Observational Study, Mon. Wea. Rev., 137, 447–468, https://doi.org/10.1175/2008MWR2467.1, 2009.

Done, J. M., Craig, G. C., Gray, S. L., Clark, P. A., and Gray, M. E. B.: Mesoscale Simulations of Organized Convection: Importance of Convective Equilibrium, Q. J. Roy. Meteor. Soc., 132, 737–756, https://doi.org/10/c4fkjs, 2006.

Done, J. M., Craig, G. C., Gray, S. L., and Clark, P. A.: Case-to-Case Variability of Predictability of Deep Convection in a Mesoscale Model, Q. J. Roy. Meteor. Soc., 138, 638–648, https://doi.org/10/b5g7mw, 2012.

Doswell, C. A., Brooks, H. E., and Maddox, R. A.: Flash Flood Forecasting: An Ingredients-Based Methodology, Wea. Forecasting, 11, 560–581, https://doi.org/10/bdhzk5, 1996.

Göbel, M.: WRFlux: V1.3.2, Zenodo [code], https://doi.org/10.5281/zenodo.5643940, 2021.

Göbel, M.: Data and Code for "Adverse Impact of Terrain Steepness on Thermally-Driven Initiation of Orographic Convection", Zenodo, https://doi.org/10.5281/zenodo.7794166, 2023.

Göbel, M., Serafin, S., and Rotach, M. W.: Numerically Consistent Budgets of Potential Temperature, Momentum, and Moisture in Cartesian Coordinates: Application to the WRF Model, Geosci. Model Dev., 15, 669–681, https://doi.org/10.5194/gmd-15-669-2022, 2022.

Griewank, P. J., Heus, T., and Neggers, R. A. J.: Size-Dependent Characteristics of Surface-Rooted Three-Dimensional Convective Objects in Continental Shallow Cumulus Simulations, J. Adv. Model Earth Sy., 14, e2021MS002612, https://doi.org/10.1029/2021MS002612, 2022.

Hagen, M., van Baelen, J., and Richard, E.: Influence of the Wind Profile on the Initiation of Convection in Mountainous Terrain, Q. J. Roy. Meteor. Soc., 137, 224–235, https://doi.org/10/bjvhrh, 2011.

Houze, R. A.: Orographic Effects on Precipitating Clouds, Rev. Geophys., https://doi.org/10/dg538r, 2012.

Imamovic, A., Schlemmer, L., and Schär, C.: Mountain Volume Control on Deep-Convective Rain Amount during Episodes of Weak Synoptic Forcing, J. Atmos. Sci., 76, 605–626, https://doi.org/10/ggw524, 2019.

Jiménez, P. A., Dudhia, J., González-Rouco, J. F., Navarro, J., Montávez, J. P., and García-Bustamante, E.: A Revised Scheme for the WRF Surface Layer Formulation, Mon. Wea. Rev., 140, 898–918, https://doi.org/10/cm98fw, 2012.

Kalthoff, N., Adler, B., Barthlott, Ch., Corsmeier, U., Mobbs, S., Crewell, S., Träumner, K., Kottmeier, Ch., Wieser, A., Smith, V., and Di Girolamo, P.: The Impact of Convergence Zones on the Initiation of Deep Convection: A Case Study from COPS, Atmos. Res., 93, 680–694, https://doi.org/10.1016/j.atmosres.2009.02.010, 2009.

Kealy, J. C., Efstathiou, G. A., and Beare, R. J.: The Onset of Resolved Boundary-Layer Turbulence at Grey-Zone Resolutions, Bound-lay. Meteorol., 171, 31–52, https://doi.org/10/ggw53d, 2019.

Keil, C., Heinlein, F., and Craig, G. C.: The Convective Adjustment Time-Scale as Indicator of Predictability of Convective Precipitation, Q. J. Roy. Meteor. Soc., 140, 480–490, https://doi.org/10/f54spm, 2014.

Kirshbaum, D. J.: Cloud-Resolving Simulations of Deep Convection over a Heated Mountain, J. Atmos. Sci., 68, 361–378, https://doi.org/10/b8kzbc, 2011.

Kirshbaum, D. J., Adler, B., Kalthoff, N., Barthlott, C., and Serafin, S.: Moist Orographic Convection: Physical Mechanisms and Links to Surface-Exchange Processes, Atmosphere, 9, 1–26, https://doi.org/10/gdq3dm, 2018.

Klemp, J. B.: A Terrain-Following Coordinate with Smoothed Coordinate Surfaces, Mon. Wea. Rev., 139, 2163–2169, https://doi.org/10/dpd3pb, 2011.

Klemp, J. B., Dudhia, J., and Hassiotis, A. D.: An Upper Gravity-Wave Absorbing Layer for NWP Applications, Mon. Wea. Rev., 136, 3987–4004, https://doi.org/10/d6hwx2, 2008.

Kumjian, M. R., Gutierrez, R., Soderholm, J. S., Nesbitt, S. W., Maldonado, P., Luna, L. M., Marquis, J., Bowley, K. A., Imaz, M. A., and Salio, P.: Gargantuan Hail in Argentina, Bull. Amer. Meteor. Soc., 101, E1241–E1258, https://doi.org/10.1175/BAMS-D-19-0012.1, 2020.

Leukauf, D., Gohm, A., and Rotach, M. W.: Quantifying Horizontal and Vertical Tracer Mass Fluxes in an Idealized Valley during Daytime, Atmos. Chem. Phys., 16, 13049–13066, https://doi.org/10/bv74, 2016.

Liu, X.-D., Osher, S., and Chan, T.: Weighted Essentially Non-oscillatory Schemes, J. Comput. Phys., 115, 200–212, https://doi.org/10/dpcvnf, 1994.

Manzato, A.: A Climatology of Instability Indices Derived from Friuli Venezia Giulia Soundings, Using Three Different Methods, Atmos. Res., 67–68, 417–454, https://doi.org/10.1016/S0169-8095(03)00058-9, 2003.

Manzato, A., Serafin, S., Miglietta, M. M., Kirshbaum, D., and Schulz, W.: A Pan-Alpine Climatology of Lightning and Convective Initiation, Mon. Wea. Rev., 150, 2213–2230, https://doi.org/10.1175/MWR-D-21-0149.1, 2022.

Marquis, J. N., Varble, A. C., Robinson, P., Nelson, T. C., and Friedrich, K.: Low-Level Mesoscale and Cloud-Scale Interactions Promoting
560   Deep Convection Initiation, Mon. Wea. Rev., 149, 2473–2495, https://doi.org/10.1175/MWR-D-20-0391.1, 2021.

Morrison, H. and Milbrandt, J. A.: Parameterization of Cloud Microphysics Based on the Prediction of Bulk Ice Particle Properties. Part I:
       Scheme Description and Idealized Tests, J. Atmos. Sci., 72, 287–311, https://doi.org/10/ggw528, 2015.

Mulholland, J. P., Nesbitt, S. W., Trapp, R. J., Rasmussen, K. L., and Salio, P. V.: Convective Storm Life Cycle and Environments near the
       Sierras de Córdoba, Argentina, Mon. Wea. Rev., 146, 2541–2557, https://doi.org/10.1175/MWR-D-18-0081.1, 2018.

565   Mulholland, J. P., Nesbitt, S. W., Trapp, R. J., and Peters, J. M.: The Influence of Terrain on the Convective Environment and Associated
       Convective Morphology from an Idealized Modeling Perspective, J. Atmos. Sci., 77, 3929–3949, https://doi.org/10/gjnqm6, 2020.

Nelson, T. C., Marquis, J., Peters, J. M., and Friedrich, K.: Environmental Controls on Simulated Deep Moist Convection Initiation Occurring
       during RELAMPAGO-CACTI, J. Atmos. Sci., 79, 1941–1964, https://doi.org/10.1175/JAS-D-21-0226.1, 2022.

Nesbitt, S. W., Salio, P. V., Ávila, E., Bitzer, P., Carey, L., Chandrasekar, V., Deierling, W., Dominguez, F., Dillon, M. E., Garcia, C. M.,
570   Gochis, D., Goodman, S., Hence, D. A., Kosiba, K. A., Kumjian, M. R., Lang, T., Luna, L. M., Marquis, J., Marshall, R., McMurdie,
       L. A., Nascimento, E. d. L., Rasmussen, K. L., Roberts, R., Rowe, A. K., Ruiz, J. J., Sabbas, E. F. M. T. S., Saulo, A. C., Schumacher,
       R. S., Skabar, Y. G., Machado, L. A. T., Trapp, R. J., Varble, A. C., Wilson, J., Wurman, J., Zipser, E. J., Arias, I., Bechis, H., and
       Grover, M. A.: A Storm Safari in Subtropical South America: Proyecto RELAMPAGO, Bull. Amer. Meteor. Soc., 102, E1621–E1644,
       https://doi.org/10.1175/BAMS-D-20-0029.1, 2021.

575   Panosetti, D., Böing, S., Schlemmer, L., and Schmidli, J.: Idealized Large-Eddy and Convection-Resolving Simulations of Moist Convection
       over Mountainous Terrain, J. Atmos. Sci., 73, 4021–4041, https://doi.org/10/f86p6r, 2016.

Panosetti, D., Schlemmer, L., and Schär, C.: Convergence Behavior of Idealized Convection-Resolving Simulations of Summertime Deep
       Moist Convection over Land, Climate Dyn., https://doi.org/10/ggw52q, 2018.

Scheffknecht, P., Serafin, S., and Grubišić, V.: A Long-Lived Supercell over Mountainous Terrain, Q. J. Roy. Meteor. Soc., 143, 2973–2986,
580   https://doi.org/10/gcshxh, 2017.

Schlemmer, L., Hohenegger, C., Schmidli, J., Bretherton, C. S., Schär, C., Schlemmer, L., Hohenegger, C., Schmidli, J., Bretherton, C. S.,
       and Schär, C.: An Idealized Cloud-Resolving Framework for the Study of Midlatitude Diurnal Convection over Land, J. Atmos. Sci., 68,
       1041–1057, https://doi.org/10/dcs8sx, 2011.

Schmidli, J.: Daytime Heat Transfer Processes over Mountainous Terrain, J. Atmos. Sci., 70, 4041–4066, https://doi.org/10/f5g23h, 2013.

585   Skamarock, W. C. and Klemp, J. B.: A Time-Split Nonhydrostatic Atmospheric Model for Weather Research and Forecasting Applications,
       J. Comput. Phys., 227, 3465–3485, https://doi.org/10/cpw3jm, 2008.

Soderholm, B., Ronalds, B., and Kirshbaum, D. J.: The Evolution of Convective Storms Initiated by an Isolated Mountain Ridge, Mon. Wea.
       Rev., 142, 1430–1451, https://doi.org/10/f54b7f, 2013.

Tucker, D. F. and Crook, N. A.: Flow over Heated Terrain. Part II: Generation of Convective Precipitation, Mon. Wea. Rev., 133, 2565–2582,
590   https://doi.org/10/bxc6fw, 2005.

Varble, A. C., Nesbitt, S. W., Salio, P., Hardin, J. C., Bharadwaj, N., Borque, P., DeMott, P. J., Feng, Z., Hill, T. C. J., Marquis, J. N., Matthews,
       A., Mei, F., Öktem, R., Castro, V., Goldberger, L., Hunzinger, A., Barry, K. R., Kreidenweis, S. M., McFarquhar, G. M., McMurdie, L. A.,
       Pekour, M., Powers, H., Romps, D. M., Saulo, C., Schmid, B., Tomlinson, J. M., van den Heever, S. C., Zelenyuk, A., Zhang, Z., and
       Zipser, E. J.: Utilizing a Storm-Generating Hotspot to Study Convective Cloud Transitions: The CACTI Experiment, Bull. Amer. Meteor.
595   Soc., 102, E1597–E1620, https://doi.org/10.1175/BAMS-D-20-0030.1, 2021.

Wagner, J. S., Gohm, A., and Rotach, M. W.: The Impact of Valley Geometry on Daytime Thermally Driven Flows and Vertical Transport Processes, Q. J. Roy. Meteor. Soc., 141, 1780–1794, https://doi.org/10/f3srnv, 2015.

Weckwerth, T. M., Wilson, J. W., Hagen, M., Emerson, T. J., Pinto, J. O., Rife, D. L., and Grebe, L.: Radar Climatology of the COPS Region, Q. J. Roy. Meteor. Soc., 137, 31–41, https://doi.org/10/dxz7gf, 2011.

600 Weinkaemmerer, J., Göbel, M., Serafin, S., Bašták Ďurán, I., and Schmidli, J.: Boundary-Layer Plumes over Mountainous Terrain in Idealized Large-Eddy Simulations, Q. J. Roy. Meteor. Soc., submitted, 2023.

Wicker, L. J. and Skamarock, W. C.: Time-Splitting Methods for Elastic Models Using Forward Time Schemes, Mon. Wea. Rev., 130, 2088–2097, https://doi.org/10/fk9n7d, 2002.

Wulfmeyer, V., Behrendt, A., Kottmeier, C., Corsmeier, U., Barthlott, C., Craig, G. C., Hagen, M., Althausen, D., Aoshima, F., Arpagaus,
605 M., Bauer, H.-S., Bennett, L., Blyth, A., Brandau, C., Champollion, C., Crewell, S., Dick, G., Girolamo, P. D., Dorninger, M., Dufournet, Y., Eigenmann, R., Engelmann, R., Flamant, C., Foken, T., Gorgas, T., Grzeschik, M., Handwerker, J., Hauck, C., Höller, H., Junkermann, W., Kalthoff, N., Kiemle, C., Klink, S., König, M., Krauss, L., Long, C. N., Madonna, F., Mobbs, S., Neininger, B., Pal, S., Peters, G., Pigeon, G., Richard, E., Rotach, M. W., Russchenberg, H., Schwitalla, T., Smith, V., Steinacker, R., Trentmann, J., Turner, D. D., van Baelen, J., Vogt, S., Volkert, H., Weckwerth, T., Wernli, H., Wieser, A., and Wirth, M.: The Convective and Orographically-induced
610 Precipitation Study (COPS): The Scientific Strategy, the Field Phase, and Research Highlights, Q. J. Roy. Meteor. Soc., 137, 3–30, https://doi.org/10/c9kc6j, 2011.

Xue, M., Droegemeier, K. K., and Wong, V.: The Advanced Regional Prediction System (ARPS) – A Multi-Scale Nonhydrostatic Atmospheric Simulation and Prediction Model. Part I: Model Dynamics and Verification, Meteorol. Atmos. Phys., 75, 161–193, https://doi.org/10/b9qwvm, 2000.

615 Zardi, D. and Whiteman, C. D.: Diurnal Mountain Wind Systems, in: Mountain Weather Research and Forecasting, Springer, https://doi.org/10.1007/978-94-007-4098-3_2, 2013.

Zimmer, M., Craig, G. C., Keil, C., and Wernli, H.: Classification of Precipitation Events with a Convective Response Timescale and Their Forecasting Characteristics, Geophys. Res. Lett., 38, https://doi.org/10/c3mz6n, 2011.